Supporting Information for "Shallow convective heating in weak temperature gradient balance explains mesoscale vertical motion in the trades"

M. Janssens[1,2], G. George[2,3], H. Schulz[4,5], Fleur Couvreux[6], Dominique Bouniol[6]

[1]Wageningen University & Research, Wageningen, The Netherlands

[2]Delft University of Technology, Delft, The Netherlands

[3]Max Planck Institute for Meteorology, Hamburg, Germany

[4]Cooperative Institute for Climate, Ocean & Ecosystem Studies (CICOES), Seattle, WA, USA

[5]University of Washington, Seattle, WA, USA

[6]CNRM, Université de Toulouse, Météo-France, CNRS, Toulouse, France

Contents of this file

Text S1. Computations of microphysical precipitation fluxes

In the ICON simulation, 3D fields of the precipitation fluxes P which appear in the main text's eqs. 5, 7, 8 and 13 are not stored at the three hourly interval of the other variables. Therefore, we attempt to reconstruct it using ICON's warm rain-sedimentation scheme, based on the two-moment implementation presented by Stevens and Seifert (2008). This scheme requires 3D fields of cloud-water specific humidity q_c, rain-water specific humidity q_r, rain-droplet number concentration N_r and density ρ. However, N_r is only available at roughly 24 hour intervals, upon model restarts. Therefore, we can evaluate P only

once a day. To still attain an estimate of P at other time instances, we approximate it as the residual of the budget for q_r itself, under the assumption that it is stationary when averaged over mesoscale blocks ($\partial_t q_{r_m} \approx 0$):

$$\frac{1}{\rho_0}\partial_z P_m \approx \frac{1}{\rho_0}\partial_z \left(\rho_0 \left(w_s' q_{r_s}'\right)_m\right) - S_{au_m} - S_{ac_m} - S_{ev_m}. \tag{1}$$

In this relation, it is assumed that only the small-scale flow transports rain water, while S_{au} and S_{ac} are the autoconversion and accretion rates, which we reconstruct from q_c, q_r and fields of effective droplet radius following Radtke, Vogel, Ament, and Naumann (2023). Rain evaporation S_{ev} also cannot be computed without N_r and is therefore (erroneously) absorbed in our definition for the divergence of P_m'.

References

Radtke, J., Vogel, R., Ament, F., & Naumann, A. K. (2023). Spatial organisation affects the pathway to precipitation in simulated trade-wind convection. *Authorea*. doi: https://doi.org/10.22541/essoar.167979635.58663858/v1

Stevens, B., & Seifert, A. (2008). Understanding macrophysical outcomes of microphysical choices in simulations of shallow cumulus convection. *Journal of the Meteorological Society of Japan. Ser. II*, *86*, 143–162.

Stevens, B., Bony, S., Farrell, D., Ament, F., Blyth, A., Fairall, C., ... others (2021). EUREC4A. *Earth System Science Data*, *13*(8), 4067–4119.

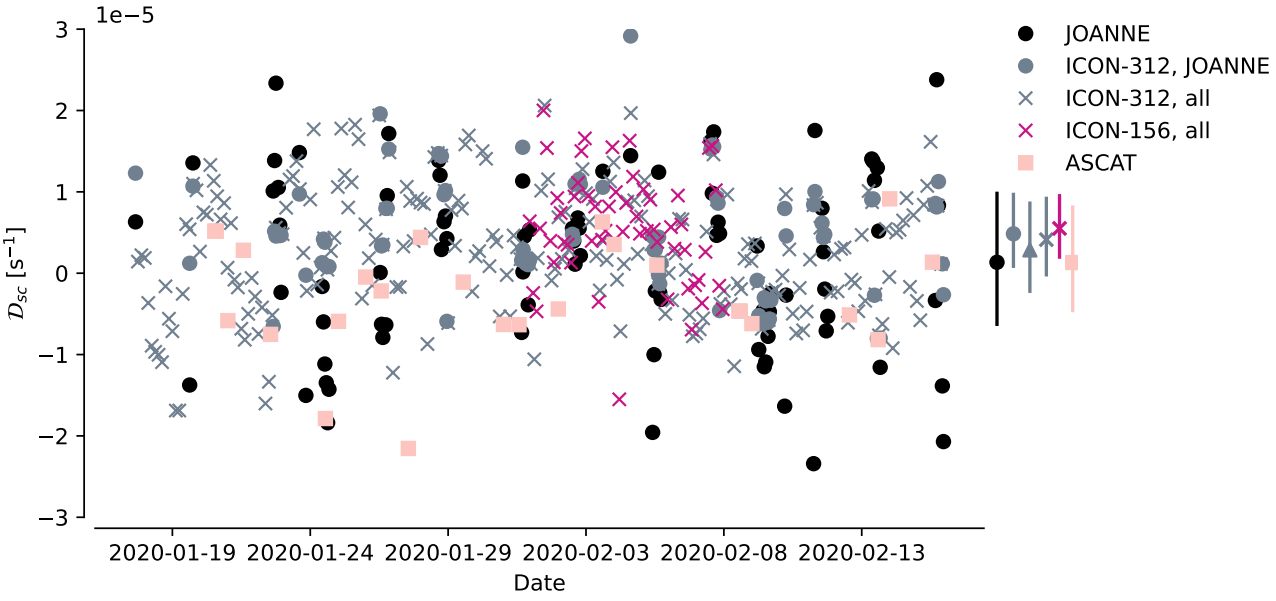

Figure S1. Estimated $\mathcal{D}_{sc}$, averaged over 200 km diameter circles i) flown during EUREC^{4}A (JOANNE), ii) extracted from ICON running at 312 m horizontal resolution, at matching locations and times (ICON-312, JOANNE), iii)/iv) averaged over the "EUREC^{4}A circle" location (Stevens et al., 2021), using all time steps in the ICON simulations running at 312 m and 156 m horizontal grid spacing resolution (ICON-312, all/ICON-156, all), and v) extracted from ASCAT over the 200 km domain in the swath nearest to the EUREC^{4}A circle. Vertical lines on the right indicate the IQR over the data sets; their marker indicates the mean. The middle line (marked by a triangle) represents the ICON-312 data statistics over the shorted period where ICON-156 ran. All simulated data sets are similar, and display a slight divergence bias with respect to ASCAT and JOANNE. Most temporal $\mathcal{D}_{sc}$ variability is contained in time scales of hours and days. No significant monthly-scale trend can be distinguished throughout the campaign.

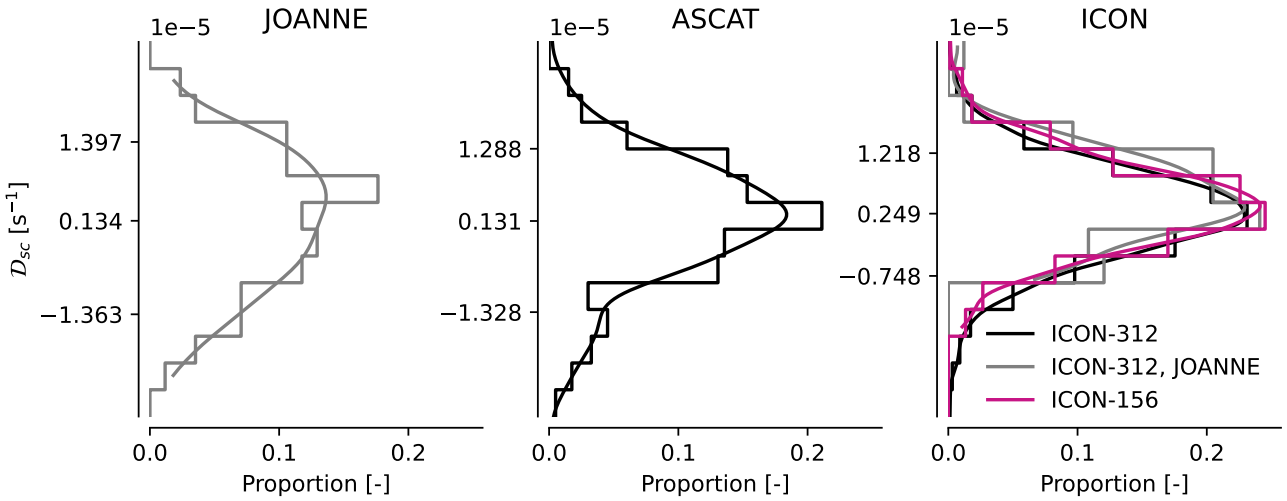

Figure S2. Probability histograms and corresponding kernel-density estimates of $\mathcal{D}_{sc}$, averaged over the lowest 600 m of 200 km diameter circles flown during EUREC^{4}A (JOANNE), over 200 km ASCAT blocks, and over the lowest 600 m of 200 km regions extracted from ICON. Three ICON curves are shown: 200 km m-blocks from ICON-312 (black) and ICON-156 (violet red), and ICON-312 composites over the locations and times when a JOANNE circle was flown (grey). Axis ticks indicate the mean, 10$^{\text{th}}$ and 90$^{\text{th}}$ percentile of each distribution (and that of ICON-312 in the right panel).

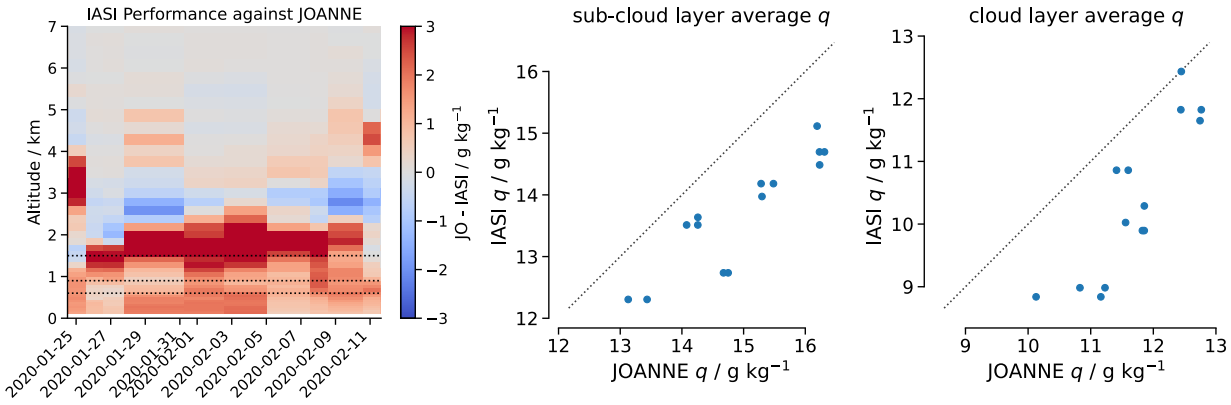

Figure S3. Left: Difference in profiles of q_v as estimated by JOANNE (JO) vs IASI, at latitude, longitude and time instances where circle-aggregated dropsonde launches best match a regridded pixel in a IASI overpass (one value per flight day). Middle and right: Comparisons of q_v averaged over the layer below 600 m ("subcloud" layer in this figure) and between 900-1500 m ("cloud layer"), for each day in the left sub-figure. Over these layers, IASI primarily displays a biased signal; its variability is qualitatively similar to JOANNE.

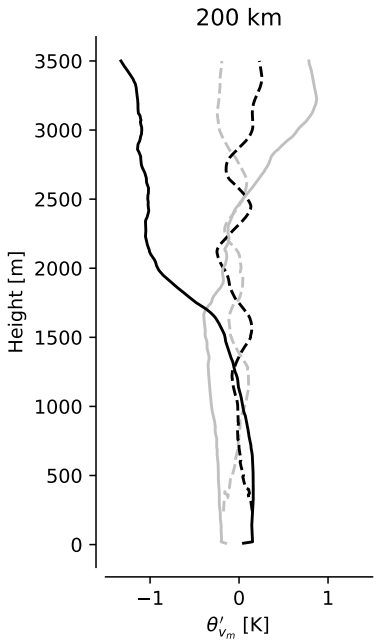

Figure S4. Temporal variability in (unbroken lines) JOANNE's θ_v around the EUREC^{4}A campaign-mean, composited by Q4 (grey) and Q1 (black) $\mathcal{D}''_{sc_m}$, and temporal variability (broken lines) in the difference between JOANNE's θ_v and the sounding network's θ_v. The latter is estimated by averaging θ_v over the soundings in the larger-scale network, on days where i) this network's vertices create a polygon whose convex hull covers an area with a square root larger than 400 km (the network should capture a larger-scale signal), ii) there are at least 5 soundings in the network during the time it took to fly a circling set, and iii) there are two circling sets. Five days (ten circling sets) satisfy these criteria. Over these circling sets, θ_{v_m} over the 200 km circle differs around 0.1 K from θ_{v_l} over the sounding network. That is, mesoscale buoyancy fluctuations are small, also above 1500 m, where the $\sim$ 1 K variability we measure in the JOANNE circles must represent larger-scale, temporal variability.

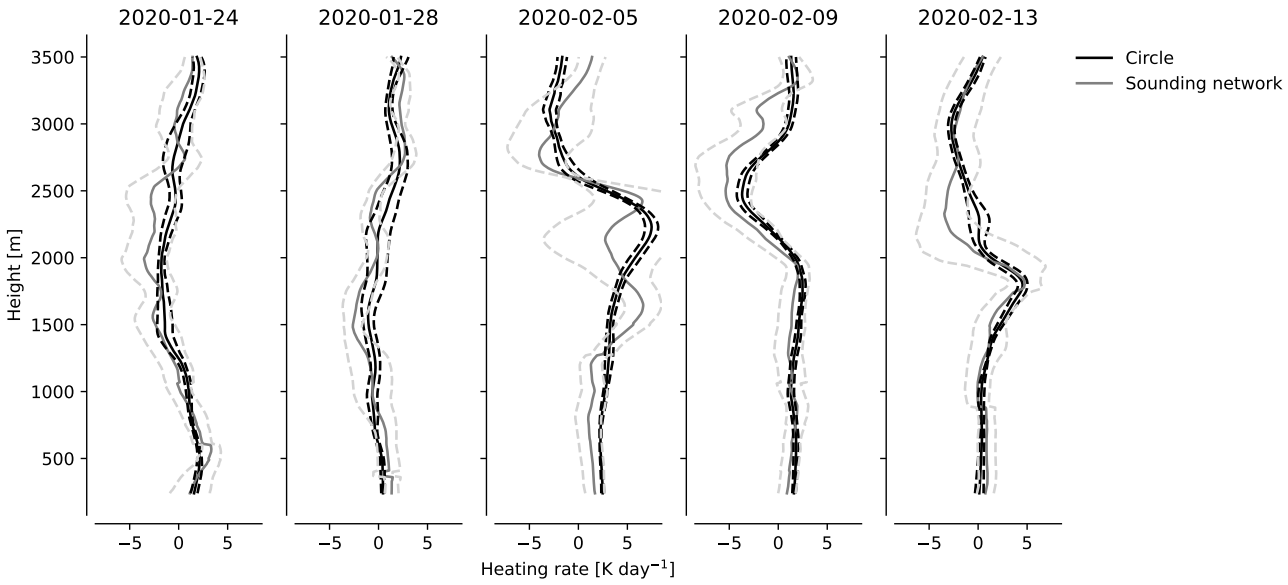

Figure S5. Estimates of the six-hourly time rate of change in θ_v between two circling sets of 3-hour averages, both in the sounding network (grey) and in JOANNE (black). $\partial_t \theta_v$ is computed by least-squares regressions against time, of i) JOANNE's circle-averaged θ_v and ii) θ_v from all individual sondes in the sounding network, on the same five days as in fig. S4. Although the heating rates vary between days, they do not differ between JOANNE and in the sounding network, to within a substantial standard regression error (marked by broken lines). In spite of this error, the main heating features in the profiles are present in both data sets. Hence, the observed heating rates appear to occur on a spatial scale larger than 200 km.

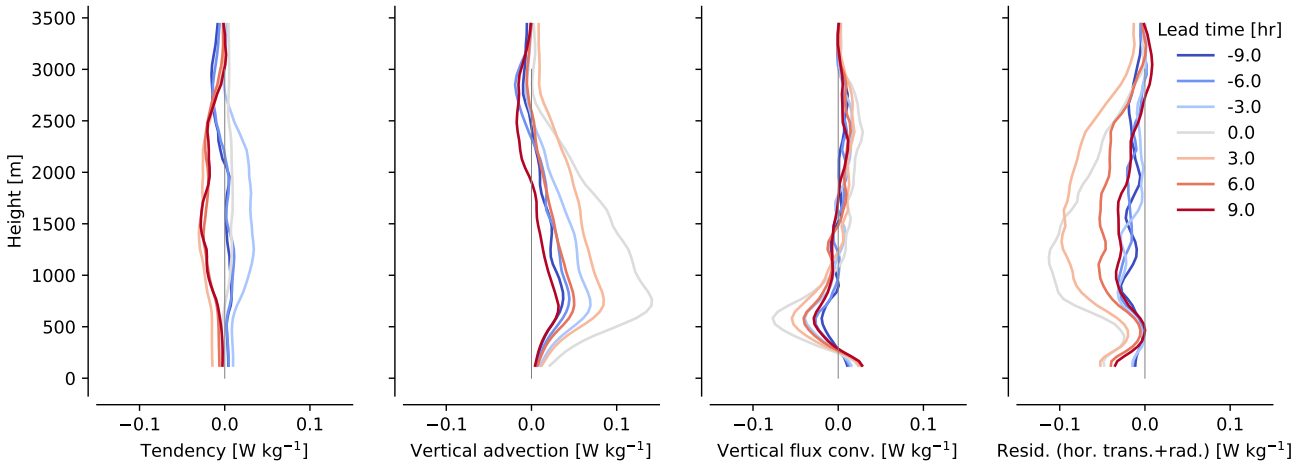

Figure S6. Budget for anomalies in Moist Static Energy (MSE) $h \approx s + L_v q_t$, where s is dry static energy, along Q1 trajectories, as in the main text's fig. 8. The figure qualitatively expresses a similar evolution as fig. 8, because in the presence of Weak Temperature Gradients, fluctuations in MSE $h' \approx L_v q_t'$. The main difference with the main text's eq. 8 is the replacement of the precipitation source, which is eliminated, with the radiative heat source $-\partial_z R$, which is subsumed under the residual.